



**HAL**  
open science

## Microstructure and mechanical properties of continuous Al<sub>2</sub>O<sub>3</sub> fiber reinforced Ni<sub>45</sub>Al<sub>45</sub>Cr<sub>7.5</sub>Ta<sub>2.5</sub> alloy (IP75) matrix composites

Yunlong Zhong, David Hajas, Weiping Hu, Hao Chen, Günter Gottstein

► **To cite this version:**

Yunlong Zhong, David Hajas, Weiping Hu, Hao Chen, Günter Gottstein. Microstructure and mechanical properties of continuous Al<sub>2</sub>O<sub>3</sub> fiber reinforced Ni<sub>45</sub>Al<sub>45</sub>Cr<sub>7.5</sub>Ta<sub>2.5</sub> alloy (IP75) matrix composites. Philosophical Magazine, 2007, 87 (07), pp.1019-1032. 10.1080/14786430601019458 . hal-00513786

**HAL Id: hal-00513786**

**<https://hal.science/hal-00513786>**

Submitted on 1 Sep 2010

**HAL** is a multi-disciplinary open access archive for the deposit and dissemination of scientific research documents, whether they are published or not. The documents may come from teaching and research institutions in France or abroad, or from public or private research centers.

L'archive ouverte pluridisciplinaire **HAL**, est destinée au dépôt et à la diffusion de documents scientifiques de niveau recherche, publiés ou non, émanant des établissements d'enseignement et de recherche français ou étrangers, des laboratoires publics ou privés.



**Microstructure and mechanical properties of continuous Al<sub>2</sub>O<sub>3</sub> fiber reinforced Ni<sub>45</sub>Al<sub>45</sub>Cr<sub>7.5</sub>Ta<sub>2.5</sub> alloy (IP75) matrix composites**

Journal:	<i>Philosophical Magazine &amp; Philosophical Magazine Letters</i>
Manuscript ID:	TPHM-06-Jul-0274.R1
Journal Selection:	Philosophical Magazine
Date Submitted by the Author:	07-Sep-2006
Complete List of Authors:	Zhong, Yunlong; Institute of Physical Metallurgy and Metal Physics, RWTH Aachen University Hajas, David; Materials Chemistry, RWTH Aachen University Hu, Weiping; Institute of Physical Metallurgy and Metal Physics, RWTH Aachen University Chen, Hao; Institute of Physical Metallurgy and Metal Physics, RWTH Aachen University Gottstein, Günter; Institute of Physical Metallurgy and Metal Physics, RWTH Aachen University
Keywords:	composite materials, mechanical properties, microstructural characterization
Keywords (user supplied):	Al <sub>2</sub> O <sub>3</sub> fiber, push-out test, composite



1  
2  
3 **Microstructure and mechanical properties of continuous Al<sub>2</sub>O<sub>3</sub> fiber**  
4  
5  
6 **reinforced Ni<sub>45</sub>Al<sub>45</sub>Cr<sub>7.5</sub>Ta<sub>2.5</sub> alloy (IP75) matrix composites**  
7  
8

9 YUNLONG ZHONG<sup>†</sup>, DAVID HAJAS<sup>‡</sup>, WEIPING HU<sup>\*†</sup>, HAO CHEN<sup>†</sup>, GÜNTER  
10  
11 GOTTSTEIN<sup>†</sup>  
12

13  
14 <sup>†</sup>Institute of Physical Metallurgy and Metal Physics, RWTH Aachen University

15  
16 Kopernikusstr. 14, D-52056 Aachen, Germany

17  
18 <sup>‡</sup>Materials Chemistry, RWTH Aachen University, Germany

19  
20 Kopernikusstr. 16, D-52056 Aachen, Germany  
21  
22  
23  
24  
25

26  
27 Single crystalline Al<sub>2</sub>O<sub>3</sub> fibers (Sapphire) coated with the NiAl alloy (IP75) by  
28  
29 physical vapor deposition (PVD) were assembled to fabricate composites by means  
30  
31 of diffusion bonding. The microstructure and chemistry of both as-coated fiber and  
32  
33 as-diffusion bonded composites were investigated by electron microscopy and  
34  
35 microanalysis. The interface shear stress for complete debonding was measured by  
36  
37 fiber push-out tests at room temperature, and the composite tensile strength was  
38  
39 measured at 900 °C and 1100 °C. An amorphous layer with a thickness of about 400  
40  
41 nm formed between the fiber and the matrix during the PVD process and was  
42  
43 maintained during diffusion bonding. A Laves phase precipitated along NiAl grain  
44  
45 boundaries in the IP75 matrix. This caused a lower tensile strength of the  
46  
47 IP75/Al<sub>2</sub>O<sub>3</sub> composite at high temperatures compared to as-cast monolithic IP75 and  
48  
49 rendered the composite useless for structural applications.  
50  
51  
52  
53

54  
55 *Keywords:* Al<sub>2</sub>O<sub>3</sub> fiber; IP75; composite; push-out test  
56  
57

---

58  
59 \*Corresponding author. Tel.: +49 241 80 26869; fax: +49 241 80 22301.

60 Email: [hu@imm.rwth-aachen.de](mailto:hu@imm.rwth-aachen.de)

## 1. Introduction

The intermetallic alloy NiAl has been extensively investigated with respect to its high temperature mechanical properties because it is considered a candidate material for structural applications owing to its high melting point, low density, good thermal conductivity and outstanding oxidation resistance [1, 2]. However, NiAl suffers from its low strength at high temperature and poor toughness at room temperature. To overcome such deficiencies, continuous ceramic fibers were incorporated into the NiAl matrix [3]. Single crystal aluminum oxide fibers (sapphire) are of particular interest because of their high modulus and strength, low density, and their excellent chemical compatibility with NiAl at high temperatures.

A higher strength at elevated temperatures with tolerable ductility at low temperatures can also be achieved by adding hard second phases to the NiAl matrix. Laves phases show outstanding high strength at high temperatures and may be used for strengthening B<sub>2</sub> ordered intermetallics, in particular NiAl. Sauthoff [4-7] studied various NiAl-Ta-Cr alloys with respect to constitution, microstructure, physical properties, and mechanical behaviour at low and high temperatures and concluded that NiAl based alloys with about 2.5 at.%Ta and 7.5 at.% Cr, referred to as IP75, are most promising for applications at temperatures above 1000 °C in view of their high hot strength and creep resistance, their tolerable brittleness at room temperature as well as excellent corrosion and thermal shock resistance at temperatures up to 1350 °C [6]. Therefore, in the current study IP75 was used as matrix material instead of NiAl to improve the mechanical properties of the matrix.

Recently, a new process was developed to fabricate continuous Al<sub>2</sub>O<sub>3</sub> fiber reinforced composites. It utilizes physical vapour deposition (PVD) to coat the fiber with the matrix material. This gives easy control over the fiber volume fraction in the composite [8-9]. In this

1  
2  
3 study,  $\text{Al}_2\text{O}_3$  fibers were coated with an IP75 matrix and then hot pressed in vacuum to  
4  
5 fabricate the composites. However, the properties of IP75 after this process are different from  
6  
7 those obtained by the casting route which has been traditionally employed to produce IP75  
8  
9 with good mechanical properties. The purpose of this investigation was to utilize IP75 as  
10  
11 matrix material and to study the microstructure and mechanical properties of sapphire fiber  
12  
13 reinforced IP75 composites fabricated by PVD and vacuum hot pressing.  
14  
15  
16  
17

## 2. Experimental procedure

18  
19  
20  
21  
22  
23  
24

25 The used single crystal sapphire fibers had a diameter of about 125  $\mu\text{m}$  and the axial direction  
26  
27 was parallel to the c-axis of  $\alpha\text{-Al}_2\text{O}_3$ . The fibers were PVD coated with layers of IP75 of  
28  
29 about 55  $\mu\text{m}$  or 25  $\mu\text{m}$  thickness corresponding to about 30% and 50% of fiber volume  
30  
31 fraction ( $V_f$ ), respectively. The coated fibers were consolidated into fully dense composites by  
32  
33 means of diffusion bonding under hot pressing. Hot pressing was carried out for 1 h at 1300  
34  
35  $^\circ\text{C}$  with a pressure of 40 MPa in vacuum ( $5 \times 10^{-3}$  Pa). The composites with  $V_f=30\%$  were  
36  
37 subjected to microstructure investigations and push-out tests; tensile tests were conducted on  
38  
39 composites with  $V_f=50\%$ . The as-coated fibers and the as-diffusion bonded composites were  
40  
41 investigated by X-ray diffraction (XRD) for phase identification and TEM for interface  
42  
43 structure observations and microanalysis employing a FEG-TEM (FEI TECNAI F20)  
44  
45 equipped with a Gatan Imaging Filter (GIF), a STEM-unit, and an energy dispersive X-ray  
46  
47 spectrometer (EDX). Small electron transparent slices with an area of about  $20 \times 10 \mu\text{m}^2$  and a  
48  
49 thickness of less than 100 nm were cut perpendicular to the fiber long axis in the interface  
50  
51 region by a focused ion beam (FIB; FEI Strata 205). The TEM analysis was carried out within  
52  
53 the specimen along the c-axis of the fiber. Details on hot pressing procedure and TEM  
54  
55 specimen preparation are given elsewhere [8].  
56  
57  
58  
59  
60

The interfacial shear stress for complete debonding was measured by fiber push-out tests

1  
2  
3 at room temperature with a micro-hardness tester. For this the specimens were sliced  
4  
5 perpendicular to the fiber axis and polished down to about 400  $\mu\text{m}$  thick. Individual fibers  
6  
7 were positioned over a 400  $\mu\text{m}$  wide groove of a substrate and subjected to an axial  
8  
9 compressive load. A diamond indenter with a spherical bottom was used. The radius of the  
10  
11 sphere was 0.2 mm. The load-displacement data were recorded with time. The interfacial  
12  
13 shear stress for complete debonding was calculated from the maximum force  $F_{\text{max}}$  by  $\tau_{\text{deb}} =$   
14  
15  $F_{\text{max}}/D\pi h$ , where  $D$  is the fiber diameter and  $h$  is the specimen height. After the push-out test  
16  
17 the fracture surfaces of the specimens were examined by SEM/EDX.  
18  
19  
20  
21  
22

23 Tensile specimens were machined with the fibers parallel to the loading direction and  
24  
25 with a reduced gage section of 40 mm length and 3.4 mm width. All tensile tests were  
26  
27 performed at high temperatures in vacuum ( $5 \times 10^{-3}$  Pa) at a strain rate of  $1 \times 10^{-4}$ /s. After the  
28  
29 tensile tests, the fracture surface was examined by SEM.  
30  
31  
32  
33  
34  
35

### 36 **3. Results**

#### 37 38 39 40 41 **3.1. Microstructure and chemistry of as-coated fibers**

42  
43  
44  
45  
46 The microstructure of an as-coated IP75/  $\text{Al}_2\text{O}_3$  fiber is shown in Fig. 1 a-b. The thickness of  
47  
48 the matrix coating is not uniform (Fig. 1a), and cracks are seen in the matrix. Columnar grains  
49  
50 extend in radial direction (Fig. 1b). Apparently the matrix is not fully dense after the PVD-  
51  
52 process.  
53  
54

55  
56 The interface structure of an as-coated fiber shown by an energy filter TEM (EFTEM)  
57  
58 image (Fig. 2a) reveals an about 400 nm thick layer between  $\text{Al}_2\text{O}_3$  fiber and IP75 matrix.  
59  
60 High resolution TEM (HRTEM) observations show an amorphous structure of the layer (Fig.  
2b-c). An element mapping by EFTEM (Fig. 2d-h) proves that the amorphous layer is oxygen

1  
2  
3 rich. Figs. 2e-f substantiate that location D in Fig. 2a is Al-oxide, and EFTEM proves that  
4 location E represents a Cu-oxide. **Since Cu was not contained in the sputter target it was**  
5 **introduced probably from the Cu-clamps on the IP75 target.** The results of an EDX analysis at  
6 locations A-E in Fig. 2a are listed in Table 1. The amorphous layer contained about 60 at.%  
7 oxygen, 10~20 at.% Ni, 20~30 at.% Al, and small amounts of Cr and Ta, **whereas in IP75**  
8 **matrix only 7.6 at.% oxygen was detected.**

9  
10 For comparison, the interface structure of an as-coated NiAl/Al<sub>2</sub>O<sub>3</sub> fiber [8] is shown in  
11 Fig. 2i. It is noticed that there is also an amorphous layer between the fiber and the NiAl  
12 matrix, although with a thickness of only 50-60 nm much thinner than in IP75 coated fibers.

### 23 **3.2. Evolution of microstructure and chemistry in IP75/Al<sub>2</sub>O<sub>3</sub> composites during diffusion** 24 **bonding**

25  
26  
27 The microstructure of an IP75/ Al<sub>2</sub>O<sub>3</sub> composite after diffusion bonding is shown in Fig. 3a.  
28 Discontinuous phases have formed at the NiAl columnar grain boundaries (Fig. 3b). At  
29 locations A-D EDX-analysis was carried out. Accordingly (see Fig. 3d) location A is  
30 comprised of NiAl, B represents a Laves phase, C is a Cr-rich phase, and D is identified as  
31 (Ni, Al)-oxide. X-ray diffraction of the matrix (Fig. 4) confirms that the bright particles in Fig.  
32 3c consist of a hexagonal or cubic Laves phase Ta(Cr, Ni, Al)<sub>2</sub>. Because both the hexagonal  
33 Laves phase C14 and the cubic Laves phase C15 exist in the matrix in the form of globular  
34 particles, no distinction was made.  $\alpha$ -Al<sub>2</sub>O<sub>3</sub>,  $\emptyset$ -NiO·16Al<sub>2</sub>O<sub>3</sub> and  $\delta$ -NiO·13Al<sub>2</sub>O<sub>3</sub> oxides were  
35 identified in the matrix. According to the Ni-Al binary phase diagram and the distribution of  
36 oxides, stable  $\alpha$ -Al<sub>2</sub>O<sub>3</sub> would form when the content of Al was greater than 17 at.% [10].  
37 Apparently in some areas, an insufficient Al content caused the formation of NiO, which  
38 reacted with Al<sub>2</sub>O<sub>3</sub> to form the metastable  $\emptyset$ -NiO·16Al<sub>2</sub>O<sub>3</sub> and  $\delta$ -NiO·13Al<sub>2</sub>O<sub>3</sub>. XRD  
39 identified also some Al<sub>2</sub>SiO<sub>5</sub> particles in the matrix, obviously introduced from impurities on  
40  
41  
42  
43  
44  
45  
46  
47  
48  
49  
50  
51  
52  
53  
54  
55  
56  
57  
58  
59  
60

1  
2  
3 the IP75 target, which resulted in the formation of  $\text{Al}_2\text{SiO}_5$  particles in the matrix during  
4  
5 diffusion bonding at  $1300^\circ\text{C}$ .  
6  
7

8 For comparison, SEM micrographs of as-cast IP75 are shown in Fig. 3e-f. The  
9  
10 microstructure of the matrix in the as-diffusion bonded composite (see Fig. 3b) is very  
11  
12 different from the microstructure of as-cast IP75 (Fig. 3e-f). Whereas in the as-diffusion  
13  
14 bonded composite hexagonal and cubic Laves phase particles of globular shape formed at the  
15  
16 NiAl columnar grain boundaries and a Cr-rich phase precipitated in the NiAl grains, in as-cast  
17  
18 IP75, NiAl grains with fine cubic Laves phase precipitates and a Cr-rich phase are surrounded  
19  
20 by hexagonal Laves phase, and a contiguous network of hexagonal Laves phase C14 formed  
21  
22 at the grain boundaries.  
23  
24  
25

26  
27 The interface structure of an IP75/ $\text{Al}_2\text{O}_3$  composite after hot pressing is shown in Fig. 5a.  
28  
29 There is still an amorphous layer at the interface (Fig. 5b-c) and many particles (dark contrast)  
30  
31 have precipitated in the layer. The cracks with darker contrast (Fig. 5a) originated from the  
32  
33 FIB-cutting in TEM preparation process. EDX-analysis (Fig. 5d) at locations A-C reveals that  
34  
35 the composition of the amorphous layer is no longer homogeneous after diffusion bonding.  
36  
37 The amorphous layer matrix is composed of about 30 at.% oxygen, 20 at.% Ni, and 40 at.%  
38  
39 Al, whereas the particles in the amorphous layer (dark contrast, such as location A in Fig. 5a)  
40  
41 are identified as (Ni, Al)-oxides which have precipitated in the amorphous layer during hot  
42  
43 pressing. Since the precipitation of (Ni,Al)-oxides consumed more oxygen than Ni and Al, the  
44  
45 oxygen content in the amorphous layer decreased. The observed (Ni, Al)-oxides indicate that  
46  
47 oxidation reactions occurred during diffusion bonding. At high temperatures, the oxidation  
48  
49 reactions progressed rapidly and thus, generated precipitates with the size of tens of  
50  
51 nanometers in the amorphous matrix.  
52  
53  
54  
55  
56  
57  
58  
59  
60

### 3.3. Mechanical properties

### 3.2.1. Results of fiber push-out tests

The measured interfacial shear stress for complete debonding  $\tau_{\text{deb}}$  in IP75/ $\text{Al}_2\text{O}_3$  and NiAl/ $\text{Al}_2\text{O}_3$  composites [8] is given in Table 2. The values scatter strongly. The average shear stress for complete debonding of IP75/ $\text{Al}_2\text{O}_3$  composites is  $217 \pm 59$  MPa, but the measured values range from 105 to 346 MPa. In comparison, the average value of  $\tau_{\text{deb}}$  for NiAl/ $\text{Al}_2\text{O}_3$  composites was  $250 \pm 42$  MPa with measurements ranging from 195 to 425 MPa. The results indicate that the average interfacial strength decreased with concomitant increase of the scatter when the matrix was changed from NiAl to IP75.

The fracture surfaces after the push-out tests (Fig. 6a-b) reveal that ridges of amorphous layer and grain boundary grooves appear on the fiber surface and the matrix inner surface, respectively. A magnified view of Fig. 6a-b, as shown in Fig. 6c-d, evaluated by EDX analysis (Fig. 6e-f) proves that location A in Fig. 6c and  $A_1$  in Fig. 6d represent the  $\text{Al}_2\text{O}_3$  fiber and the NiAl matrix, respectively, whereas B and  $B_1$  belong to the amorphous layer which existed between fiber and matrix prior to the fiber push-out test.

### 3.2.2. Tensile tests

Characteristic stress-strain diagrams for as-cast IP75 and IP75/ $\text{Al}_2\text{O}_3$  with 50% fiber volume fraction at 900 °C and 1100 °C are shown in Fig. 7a. At 1100 °C as-cast IP75 reveals good ductility (elongation above 20%) and a tensile strength of 136MPa. By contrast, the IP75/ $\text{Al}_2\text{O}_3$  composite had only a tensile strength of about 123 MPa at 900 °C and 107 MPa at 1100 °C.

The fracture surfaces of the IP75/ $\text{Al}_2\text{O}_3$  composite and the as-cast IP75 after a tensile test at 1100 °C are shown in Figs. 7b and c, respectively. In the IP75 matrix of the composite the

1  
2  
3 Laves phase particles acted as fracture origin at the grain boundaries and thus caused the  
4  
5 entirely intergranular fracture, whereas in as-cast IP75 ductile fracture occurred.  
6  
7  
8  
9

#### 10 11 **4. Discussion**

##### 12 13 14 15 16 ***4.1. As-coated IP75/Al<sub>2</sub>O<sub>3</sub> fiber***

17  
18  
19  
20  
21 The observed amorphous phase at the IP75/ Al<sub>2</sub>O<sub>3</sub> interface is not a thermodynamic  
22  
23 equilibrium phase of the alloy system; rather it is a processing artifact, **resulting from the**  
24  
25 **incorporation of Al and Ni with the remaining moisture of the residual gas in the reaction**  
26  
27 **chamber during the vapor-phase growth in high vacuum during the initial stage of PVD**  
28  
29 **process and the surface oxide of the sputter target used for the PVD process.** Owing to  
30  
31 multiple scattering of the sputtered atoms in the gas phase and their resulting low kinetic  
32  
33 energy, an amorphous phase can form [11].  
34  
35  
36

37  
38 Sputter deposition is a highly exothermic process [12]. Since heat transfer from the fibers  
39  
40 to the surrounding is limited, the release of latent heat during deposition caused a significant  
41  
42 increase of the temperature of the fiber and the deposited matrix. During the cooling process  
43  
44 after coating, thermal residual stresses developed due to different CTEs of fiber and matrix  
45  
46 (NiAl CTE:  $15 \times 10^{-6}$ ,  $\alpha$ -Al<sub>2</sub>O<sub>3</sub> CTE:  $9.5 \times 10^{-6}$  [13]) **and caused the cracks in the matrix as**  
47  
48 **evident from Fig. 1a. And the non-uniform coating around the fiber caused bending of the**  
49  
50 **fibers.**  
51  
52  
53

54  
55  
56 ***4.2. The precipitation mechanism of Laves phases and Cr-rich phase in as-diffusion bonded***  
57  
58 ***IP75/Al<sub>2</sub>O<sub>3</sub> composite and as-cast IP75 and their effect on tensile strength***  
59  
60

1  
2  
3 The chemical analysis showed that the IP75 matrix is mainly composed of B2 NiAl,  
4 hexagonal C14 and cubic C15 Laves phases  $Ta(Cr, Ni, Al)_2$ , a Cr-rich phase and (Ni,Al)-  
5 oxides. The binary Laves phase  $TaCr_2$  has a large homogeneity range to both sides of the  
6 stoichiometric composition [14, 15]. They can dissolve comparably large amounts of third  
7 elements without changing their crystallographic structure type. Hence,  $Ta(Cr, Ni, Al)_2$   
8 corresponds to the binary Laves phase  $TaCr_2$ , where Ni and Al primarily substitute for Cr, i.e.  
9 occupy the same kind of sublattice sites in this Laves phase. The Ni/Al ratio can be varied  
10 within broad limits according to the ternary phase diagram [16, 17]. The NiAl phase in NiAl-  
11 Ta alloys can dissolve up to about 3 at.% Cr [6]. However, the Cr content in IP75 is 7.5 at.%.  
12 The surplus Cr, therefore, is precipitated in a disordered Cr-rich phase. Its low strength can be  
13 used for improving the mechanical behaviour, especially the ductility and toughness, of NiAl  
14 alloys.  
15  
16  
17  
18  
19  
20  
21  
22  
23  
24  
25  
26  
27  
28  
29  
30

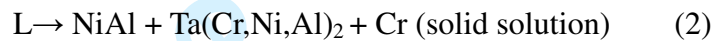
31 In the current study, columnar NiAl grains formed during PVD. During diffusion  
32 bonding, the hexagonal C14 and the cubic C15 Laves phases were produced by:  
33



35  
36  
37  
38 Therefore, the hexagonal C14 and cubic C15 Laves phases formed at NiAl grain boundaries  
39 by solid state phase transformations, even though for the hexagonal Laves phase the hot  
40 pressing temperature (1300 °C) was by far lower than the eutectic transformation temperature  
41 (about 1638 °C). Thus, globular hexagonal and cubic Laves phase precipitates formed along  
42 the columnar grain boundaries of NiAl, whereas a Cr-rich phase precipitated in the NiAl  
43 matrix. The Laves phase transformation from hexagonal C14  $Ta(Cr, Ni, Al)_2$  to cubic C15  
44  $Ta(Cr, Ni, Al)_2$  via a eutectoid reaction at a lower temperature is considered to occur by shear,  
45 and the shear transformation kinetics are believed to be dictated by the temperature  
46 dependence of dislocation mobility [18]. Under normal solidification conditions, the  
47 C14→C15 transformation tends to be sluggish and is often suppressed, thus the C14 structure  
48 can be retained even to room temperature in as-cast microstructures [18-20]. In a previous  
49  
50  
51  
52  
53  
54  
55  
56  
57  
58  
59  
60

1  
2  
3 study [21] it was observed in as-cast IP75 that rod-shaped cubic C15 precipitated to a large  
4 extent in NiAl grains only during annealing in a temperature range of 1000~1300 °C owing to  
5 a supersaturation of Ta (about 0.6~0.7 at.%) in the NiAl matrix (the solubility of Ta in NiAl is  
6 about 0.2 at.% in that temperature range). Moreover, during this C15 Laves phase  
7 precipitation no detectable dissolution of C14 Laves phase was observed. This indicates that  
8 the hexagonal C14 Laves phase is actually the stable phase component.  
9  
10  
11  
12  
13  
14

15  
16  
17 However, the as-cast IP75 was cast at a high temperature above 1700°C [22]. During  
18 solidification, a eutectic reaction occurred to form the C14 Laves phase as a eutectic  
19 microconstituent or a primary phase from the liquid:  
20  
21  
22  
23



24  
25  
26 As a consequence, the NiAl grains with fine precipitates of the Cr-rich phase and the cubic  
27 C15 Laves phase are surrounded by hexagonal C14 Laves phase, which covers the grain  
28 boundaries more or less completely to form a skeleton.  
29  
30  
31  
32  
33

34 Comparing the microstructure of IP75 in both the cast and the deposited state, it is  
35 obvious that the eutectic hexagonal Laves phase formed in the as-cast alloy will hinder  
36 deformation more effectively than the small globular hexagonal and cubic Laves phase  
37 precipitates in the grain boundaries of the deposited and diffusion bonded state. Hence, the  
38 microstructure of the IP75 matrix in the as-diffusion bonded IP75/Al<sub>2</sub>O<sub>3</sub> composite causes a  
39 low strength of the IP75 matrix and consequently a low strength of the composite. Even the  
40 reinforcement by Al<sub>2</sub>O<sub>3</sub> fibers cannot compensate the loss of strength so that IP75/Al<sub>2</sub>O<sub>3</sub>  
41 composites have a lower tensile strength than as-cast IP75. In essence, IP75 fabricated by a  
42 PVD process is not suitable as matrix material for fiber reinforced composites with high  
43 strength and toughness.  
44  
45  
46  
47  
48  
49  
50  
51  
52  
53  
54  
55  
56  
57  
58  
59  
60

#### ***4.3. Interfacial properties and debonding mechanisms***

1  
2  
3 The shear stress for complete debonding in  $\text{Al}_2\text{O}_3$  fiber-reinforced IP75 and NiAl composites,  
4 fabricated by a fiber coating process, was determined to be  $217\pm 59$  and  $250\pm 42$  MPa  
5 respectively. These values are of the same order as reported for sapphire/NiAl composites  
6 fabricated by binder-free powder metallurgy methods ( $283\pm 53$  MPa) [23]. The high  
7 debonding shear stress was attributed to the adherence of  $\text{Al}_2\text{O}_3$  fibers to NiAl and the  
8 clamping pressure from the matrix on the fiber which builds up during cooling after diffusion  
9 bonding owing to the different CTEs of fiber and matrix [8]. The lower interfacial shear  
10 strength in IP75-composites compared to NiAl-composites [8] is apparently due to the  
11 amorphous layer between fiber and matrix, which affects the debonding mechanism. In  
12 NiAl/ $\text{Al}_2\text{O}_3$  composites, interface debonding took place at the boundary between the NiAl  
13 matrix and the amorphous layer [8]. By contrast, in IP75/ $\text{Al}_2\text{O}_3$  composites every grain  
14 boundary groove on the NiAl surface is complemented by a corresponding ridge of the  
15 amorphous layer on the fiber surface (Fig. 6). During the fiber push-out test, the IP75/ $\text{Al}_2\text{O}_3$   
16 interface is subjected to an interfacial shear stress, and a stress concentration is generated at  
17 the grain boundary grooves which causes crack initiation and propagation in the amorphous  
18 layer (Fig. 8). After the push-out test, the about 400 nm thick amorphous layer has been split:  
19 one part sticks to the fiber surface in the form of ridges; the counterpart forms the inner  
20 surface of the matrix. In essence, interface debonding occurred in the amorphous layer along  
21 NiAl grain boundary grooves, which decreased the interfacial shear strength and thus the  
22 strength of the composite.  
23  
24  
25  
26  
27  
28  
29  
30  
31  
32  
33  
34  
35  
36  
37  
38  
39  
40  
41  
42  
43  
44  
45  
46  
47  
48  
49  
50  
51

## 52 5. Conclusions

53  
54  
55  
56  
57  
58 The microstructure and mechanical properties of both as-coated and as-diffusion bonded  
59 IP75/ $\text{Al}_2\text{O}_3$  composites were investigated. An amorphous interlayer with a thickness of about  
60 400 nm was formed between fiber and matrix after the PVD process and maintained after

1  
2  
3 diffusion bonding. The IP75 matrix produced by PVD and diffusion bonding had a less  
4 favorable microstructure than as-cast IP75 with respect to mechanical properties, and  
5 therefore, is not suitable for high temperature composites.  
6  
7  
8  
9

10 The shear stress for complete debonding of IP75/Al<sub>2</sub>O<sub>3</sub> composites was found to decrease  
11 to 217±59 MPa compared to 250±42 MPa for NiAl/Al<sub>2</sub>O<sub>3</sub> composites. Interface debonding  
12 occurred in the thick amorphous layer, and is different from the debonding mechanism in  
13 NiAl/Al<sub>2</sub>O<sub>3</sub> composites.  
14  
15  
16  
17  
18  
19  
20  
21

## 22 Acknowledgements

23  
24  
25  
26  
27 The authors acknowledge the financial support of the Deutsche Forschungsgemeinschaft  
28 through the collaborative research center SFB 561: "Thermally Highly Loaded Porous and  
29 cooled Multi-layer Systems for Combined Cycle Power Plants". We also highly appreciate the  
30 technical support from our colleagues T. Burlet and Dipl.-Ing. S. Bhaumik in the fabrication  
31 of the composites.  
32  
33  
34  
35  
36  
37  
38  
39  
40

## 41 References

- 42  
43  
44  
45 [1] R. Darolia, J. Met. **43** 44 (1991).  
46  
47 [2] S. N. Tewari, R. Asthana, R. Tiwari. R.R. Bowman, J. Smith, Metall. and Mater. Trans. A  
48 **26** 477(1995).  
49  
50  
51 [3] J.M. Yang, S.M. Jeng, K. Bain, R.A. Amoto, Acta Mater. **45** 295 (1997).  
52  
53 [4] B.Zeumer, G. Sauthoff, Intermetallics **5** 563 (1997).  
54  
55 [5] B.Zeumer, G. Sauthoff, Intermetallics **5** 641 (1997).  
56  
57 [6] B.Zeumer, G. Sauthoff, Intermetallics **6** 451 (1998).  
58  
59 [7] B.Zeumer, G. Sauthoff, Intermetallics **7** 889 (1999).  
60

- 1  
2  
3 [8] W. Hu, T. Weirich, B. Hallstedt, H. Chen, Y. Zhong, G. Gottstein, *Acta Mater.* **54** 2473  
4  
5 (2006).  
6  
7  
8 [9] K. Wen, K. Reichert, W. Hu, M. Frommert, G. Gottstein, *Mater. Sci. Eng. A* **367** 33 (2004).  
9  
10 [10] P. Nash, M.F. Singleton, J.L. Murry, *Phase Diagram of Binary Nickel Alloys* (ASM  
11  
12 International, Metals Park, OH, 1991).  
13  
14 [11] *Sputter Deposition*, edited by D. Westwood, AVS Education Committee Book Series, Vol.  
15  
16 2, New York, 285 pages, \$95, hardback (ISBN: 0-7354-0105-5).  
17  
18 [12] G.B. Thompson, R. Banerjee, X.D. Zhang, P.M. Anderson, H.L. Fraser, *Acta Mater.* **50**  
19  
20 643 (2002).  
21  
22 [13] S.N. Tewari, R. Asthana, R.D. Noebe, *Metall. Trans. A* **24** 2119 (1993).  
23  
24 [14] F. Stein, M. Palm, G. Sauthoff, *Intermetallics* **12** 713 (2004).  
25  
26 [15] F. Stein, M. Palm, G. Sauthoff, *Intermetallics* **13** 1056 (2005).  
27  
28 [16] M. Palm, W. Sanders, G. Sauthoff, *Z. Metallkde* **87** 390 (1996).  
29  
30 [17] F. Scheppe, P.R. Sahn, W. Hermann, U. Paul, J. Preuhs, *Mater. Sci. and Eng. A* **329-331**  
31  
32 596 (2002).  
33  
34 [18] K.S. Kumar, L. Pang, C.T. Liu, J. Horton, E.A. Kenik, *Acta. Mater.* **48** 911 (2000).  
35  
36 [19] K.S. Kumar, P.M. Hazzledine, *Intermetallics* **12** 763 (2004).  
37  
38 [20] F. Zhang, S.L. Chen, Y.A. Chang, W.A. Oates, *Intermetallics* **9** 1079 (2001).  
39  
40 [21] J. Lin, W. Hu, G. Gottstein, Poster presented at Materials Week, Munich, Germany, 21-23  
41  
42 September (2004).  
43  
44 [22] D.R. Johnson, B.F. Oliver, R.D. Noebe, J.D. Whittenberger, *Intermetallics* **3** 493 (1995).  
45  
46 [23] J.I. Eldridge, D.R. Wheeler, R.R. Bowman, *J. Mater. Res.* **12** 2191 (1997).  
47  
48  
49  
50  
51  
52  
53  
54  
55  
56  
57  
58  
59  
60

1  
2  
3  
4  
5  
6  
7  
8  
9  
10  
11  
12  
13  
14  
15  
16  
17  
18  
19  
20  
21  
22  
23  
24  
25  
26  
27  
28  
29  
30  
31  
32  
33  
34  
35  
36  
37  
38  
39  
40  
41  
42  
43  
44  
45  
46  
47  
48  
49  
50  
51  
52  
53  
54  
55  
56  
57  
58  
59  
60

**Tables with captions**

Tab. 1 Semi-quantitative results of EDX-analysis in Fig. 2(a) (at.%)

position	Ni	Al	O	Cr	Ta	Cu
A	11.5	25.4	58.6	2.5	2.0	0.0
B	0.0	47.3	52.7	0.0	0.0	0.0
C	51.0	30.3	7.6	6.5	4.7	0.0
D	0.0	46.4	53.6	0.0	0.0	0.0
E	0.0	0.0	14.4	0.0	0.0	85.6

Tab. 2 Measured interfacial shear stress for complete debonding

Interfacial shear stress (MPa)	IP75/Al <sub>2</sub> O <sub>3</sub>	NiAl/Al <sub>2</sub> O <sub>3</sub> [8]
	217±59	250±42

## Figure captions

Fig. 1: SEM micrographs (secondary electron image, SEI) of the as-coated IP75/Al<sub>2</sub>O<sub>3</sub> fiber. (a) non-uniformity of matrix coating, (b) columnar matrix grains after PVD.

Fig. 2: (a) Bright field EFTEM image of the interface structure of as-coated IP75/Al<sub>2</sub>O<sub>3</sub>. Results of STEM/EDX-analysis at locations A to E are listed in Table 1. (b-c) HRTEM micrographs reveal the fine structure of the interface between IP75 and the amorphous layer and between the amorphous layer and Al<sub>2</sub>O<sub>3</sub> in as-coated IP75/Al<sub>2</sub>O<sub>3</sub> fiber, (d-h) EFTEM element mapping of the interface area shown in Fig. 2a. (i) Bright field EFTEM image of the interface structure of as-coated NiAl/Al<sub>2</sub>O<sub>3</sub> fiber [8].

Fig. 3: SEM micrographs (SEI) of the microstructure of IP75/ Al<sub>2</sub>O<sub>3</sub> composite after diffusion bonding and in as-cast IP75. (a) Transverse section of the composite, (b) discontinuous Laves phase formed at NiAl columnar grain boundaries, (c) magnified view of the IP75 matrix, (d) results of semi-quantitative EDX-analysis at locations A-D in Fig. 3c, (e) network of Laves phase formed at NiAl grain boundaries in as-cast IP75, (f) cubic Laves phase and Cr-rich particles precipitate in the NiAl grains in as-cast IP75.

Fig. 4: Diffractogram and phase identification of the matrix of an as-diffusion bonded IP75/Al<sub>2</sub>O<sub>3</sub> composite.

Fig. 5 (a) EFTEM micrograph of the interface structure of an as-diffusion bonded IP75/Al<sub>2</sub>O<sub>3</sub> composite, (b-c) HRTEM micrographs reveal the fine structure of the interface between NiAl and amorphous layer and between amorphous layer and Al<sub>2</sub>O<sub>3</sub> in as-diffusion bonded IP75/Al<sub>2</sub>O<sub>3</sub> composite, (d) results of semi-quantitative STEM/EDX-analysis at locations A-C in Fig. 5a.

Fig. 6: SEM micrographs (SEI) of an IP75/Al<sub>2</sub>O<sub>3</sub> composite after push-out tests: (a) fiber surface, (b) matrix inner surface, (c-d) magnified views of a and b, respectively. (e-f) results of semi-quantitative EDX-analysis at locations A-B in Fig. 6c and A<sub>1</sub>-B<sub>1</sub> in Fig. 6d

1  
2  
3 respectively.  
4  
5

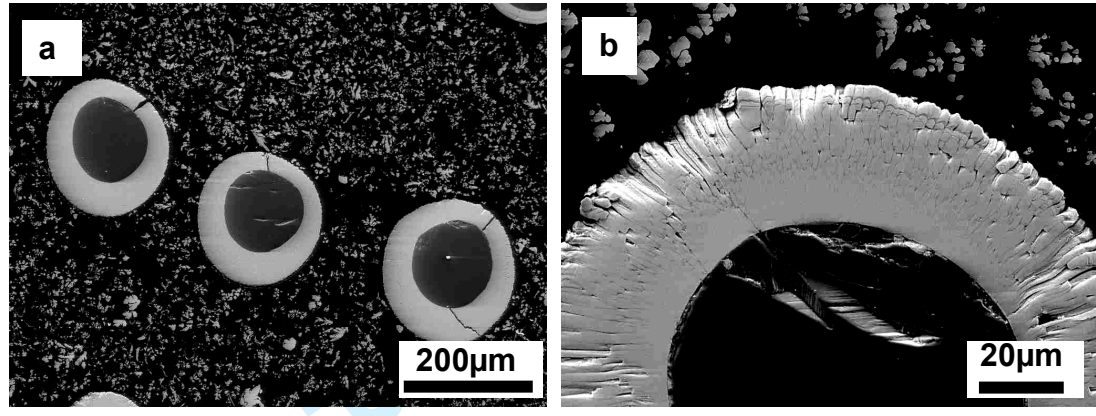
6 Fig.7: Results of tensile tests at 900 °C and 1100°C at a strain rate of  $10^{-4} \text{ s}^{-1}$ . (a) Typical  
7 stress-strain diagrams of as-cast IP75 and IP75/ $\text{Al}_2\text{O}_3$  with 50% fiber volume fraction, (b)  
8 fracture surface of IP75 matrix in IP75/ $\text{Al}_2\text{O}_3$  composite and (c) fracture surface of as-cast  
9 IP75 after tensile test at 1100 °C, SEM/SEI-image.  
10  
11  
12  
13  
14

15  
16 Fig. 8: Model of grain boundary grooving and interface debonding during fiber push-out test  
17 in IP75/ $\text{Al}_2\text{O}_3$  composite.  
18  
19  
20  
21  
22  
23  
24  
25  
26  
27  
28  
29  
30  
31  
32  
33  
34  
35  
36  
37  
38  
39  
40  
41  
42  
43  
44  
45  
46  
47  
48  
49  
50  
51  
52  
53  
54  
55  
56  
57  
58  
59  
60

1  
2  
3  
4  
5  
6  
7  
8  
9  
10  
11  
12  
13  
14  
15  
16  
17  
18  
19  
20  
21  
22  
23  
24  
25  
26  
27  
28  
29  
30  
31  
32  
33  
34  
35  
36  
37  
38  
39  
40  
41  
42  
43  
44  
45  
46  
47  
48  
49  
50  
51  
52  
53  
54  
55  
56  
57  
58  
59  
60

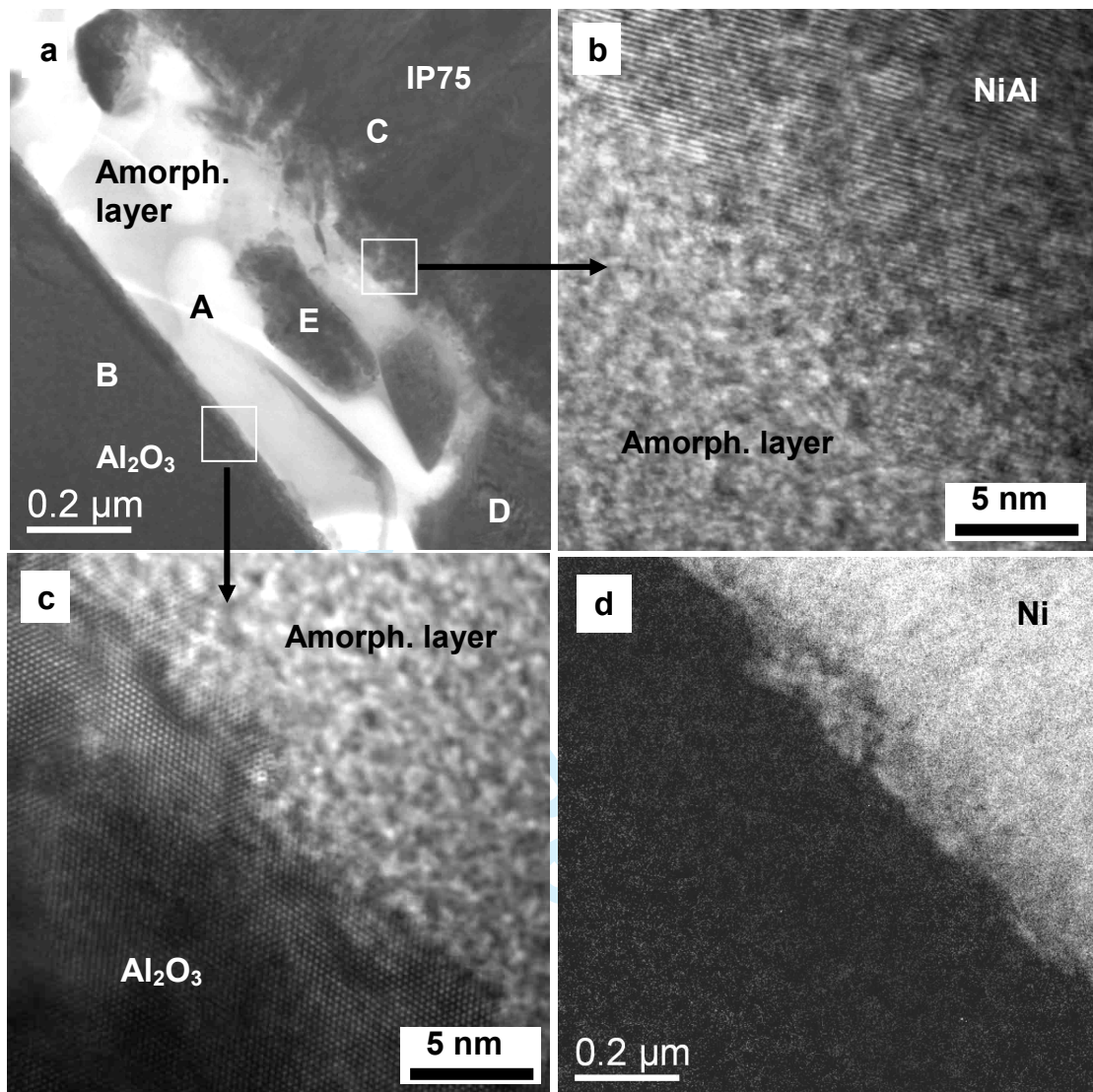
Figures

Fig. 1



Peer Review Only

Fig. 2



1  
2  
3  
4  
5  
6  
7  
8  
9  
10  
11  
12  
13  
14  
15  
16  
17  
18  
19  
20  
21  
22  
23  
24  
25  
26  
27  
28  
29  
30  
31  
32  
33  
34  
35  
36  
37  
38  
39  
40  
41  
42  
43  
44  
45  
46  
47  
48  
49  
50  
51  
52  
53  
54  
55  
56  
57  
58  
59  
60

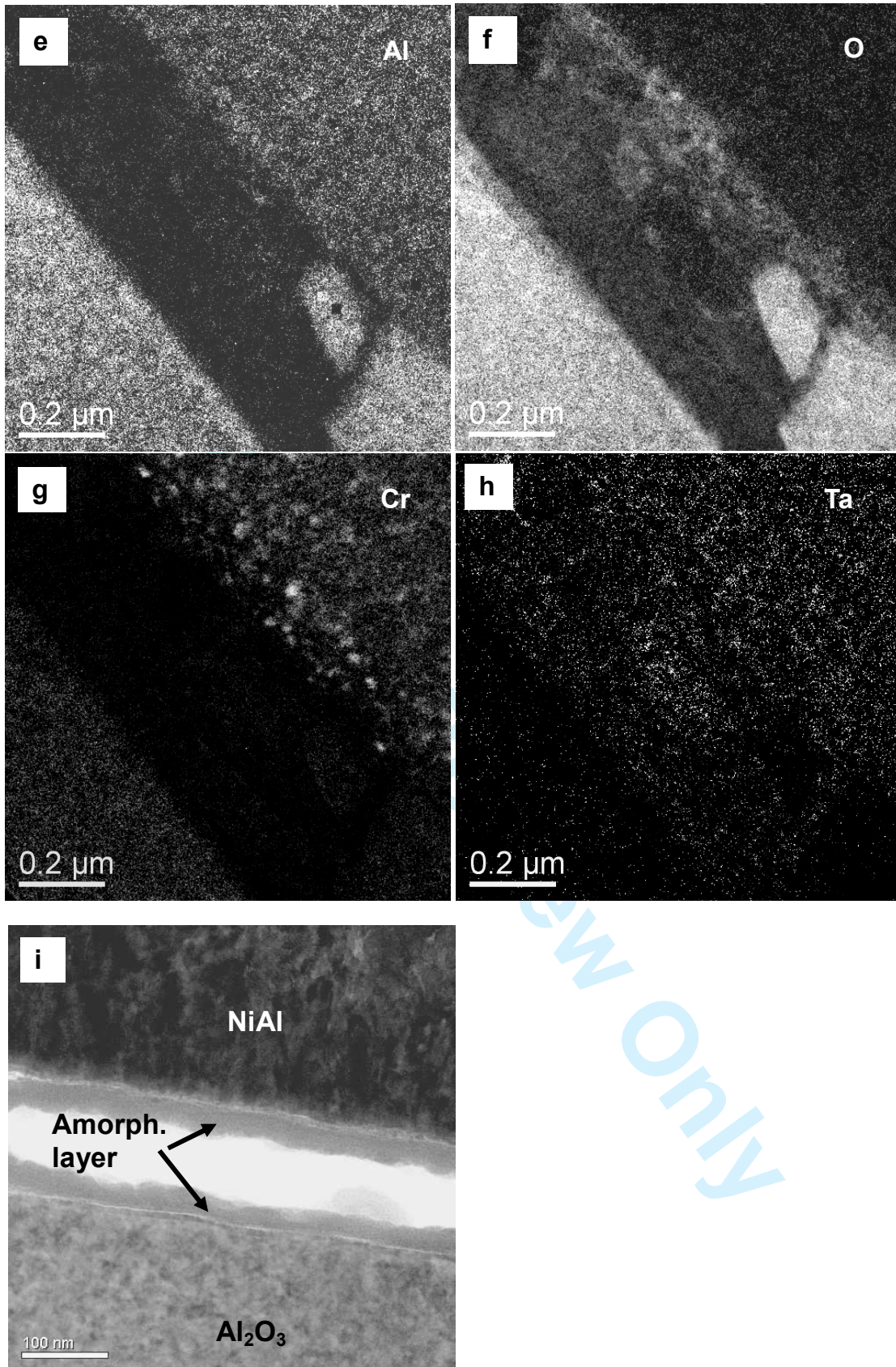


Fig. 3

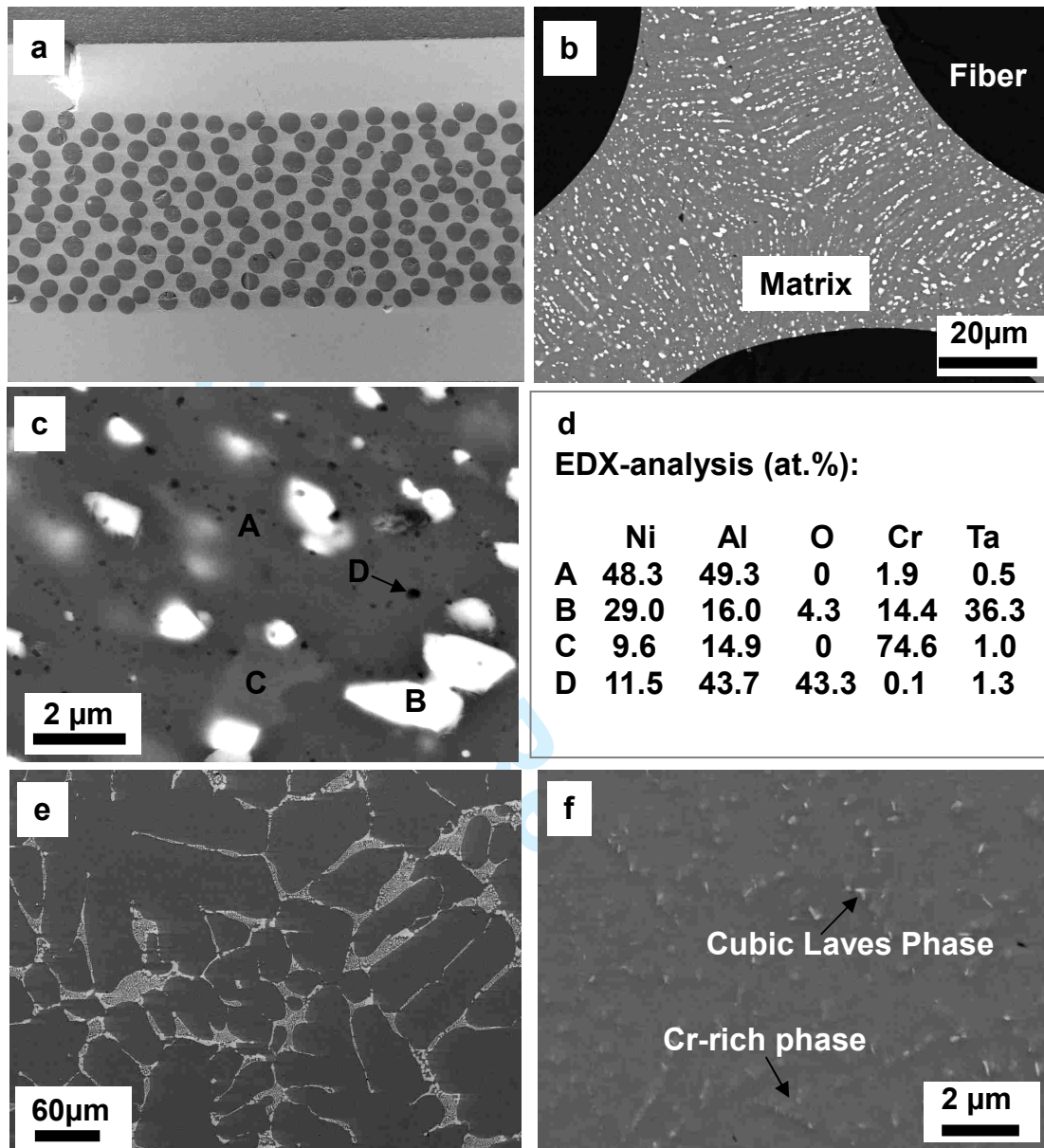


Fig. 4

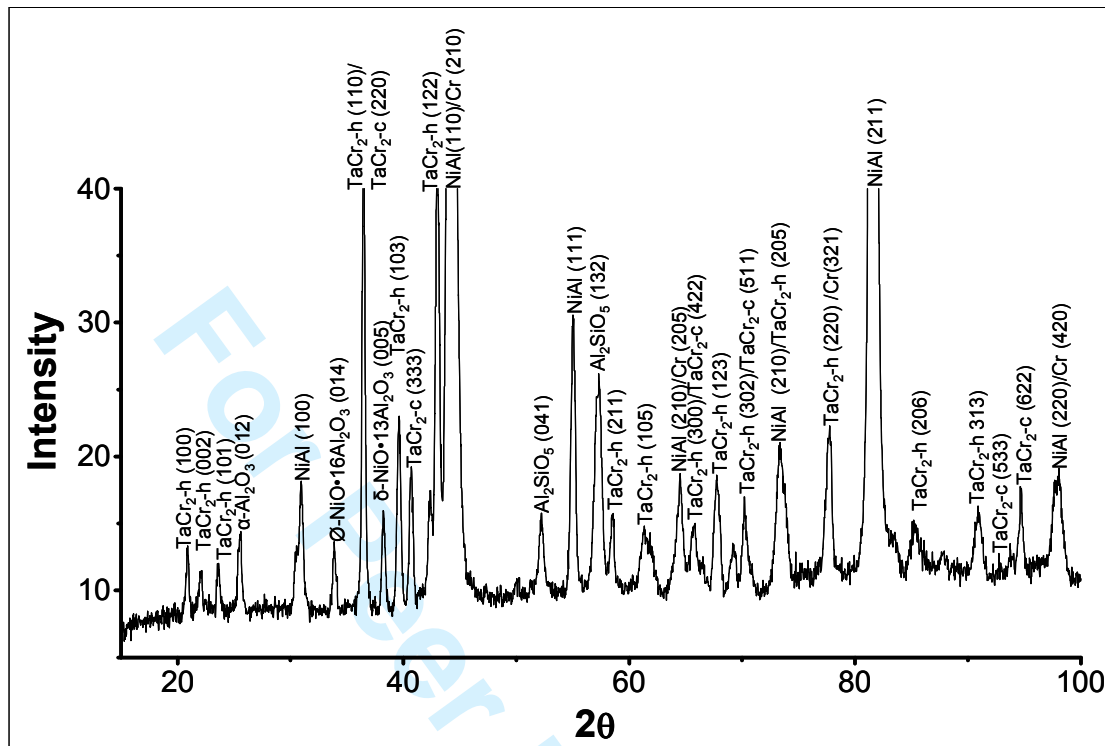


Fig. 5

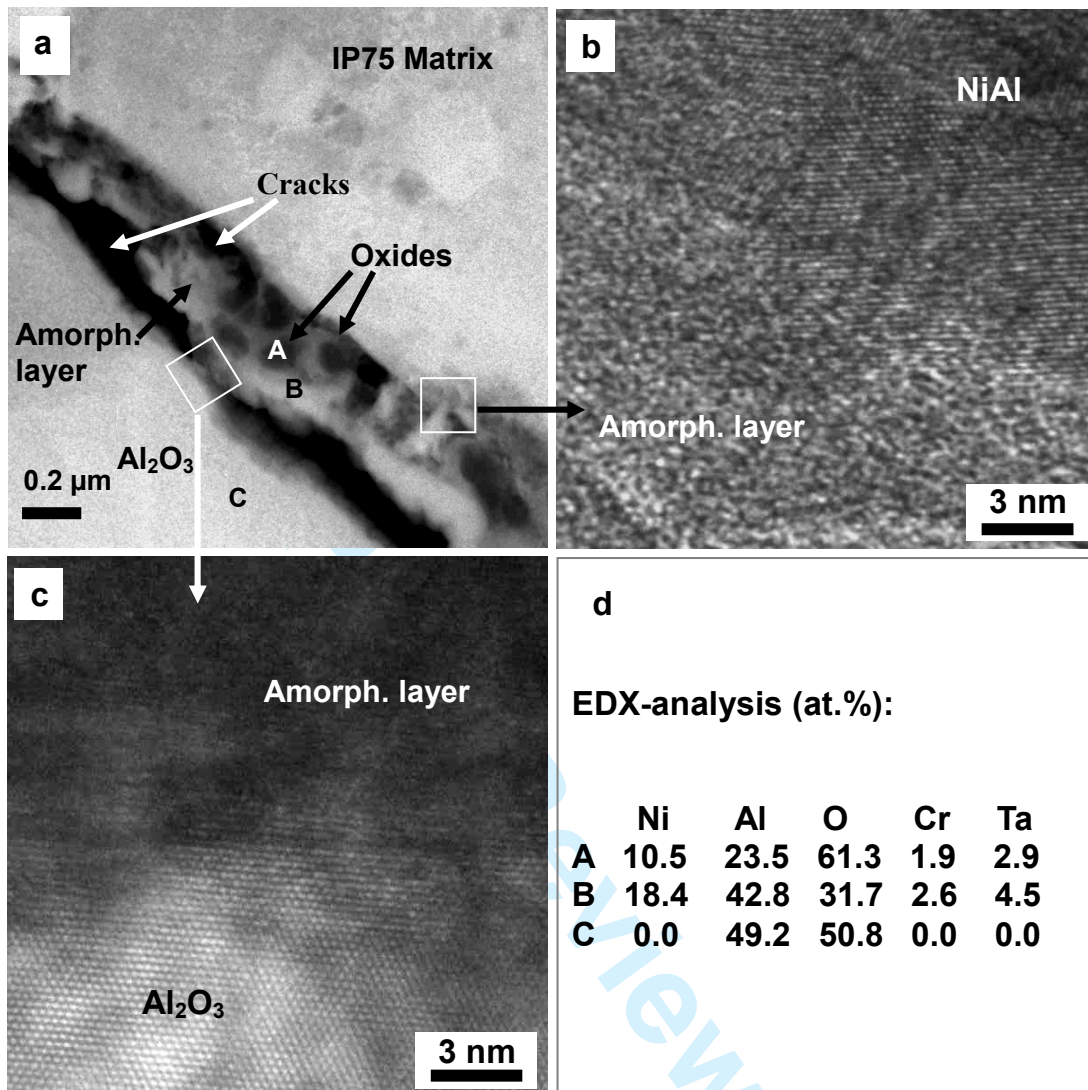
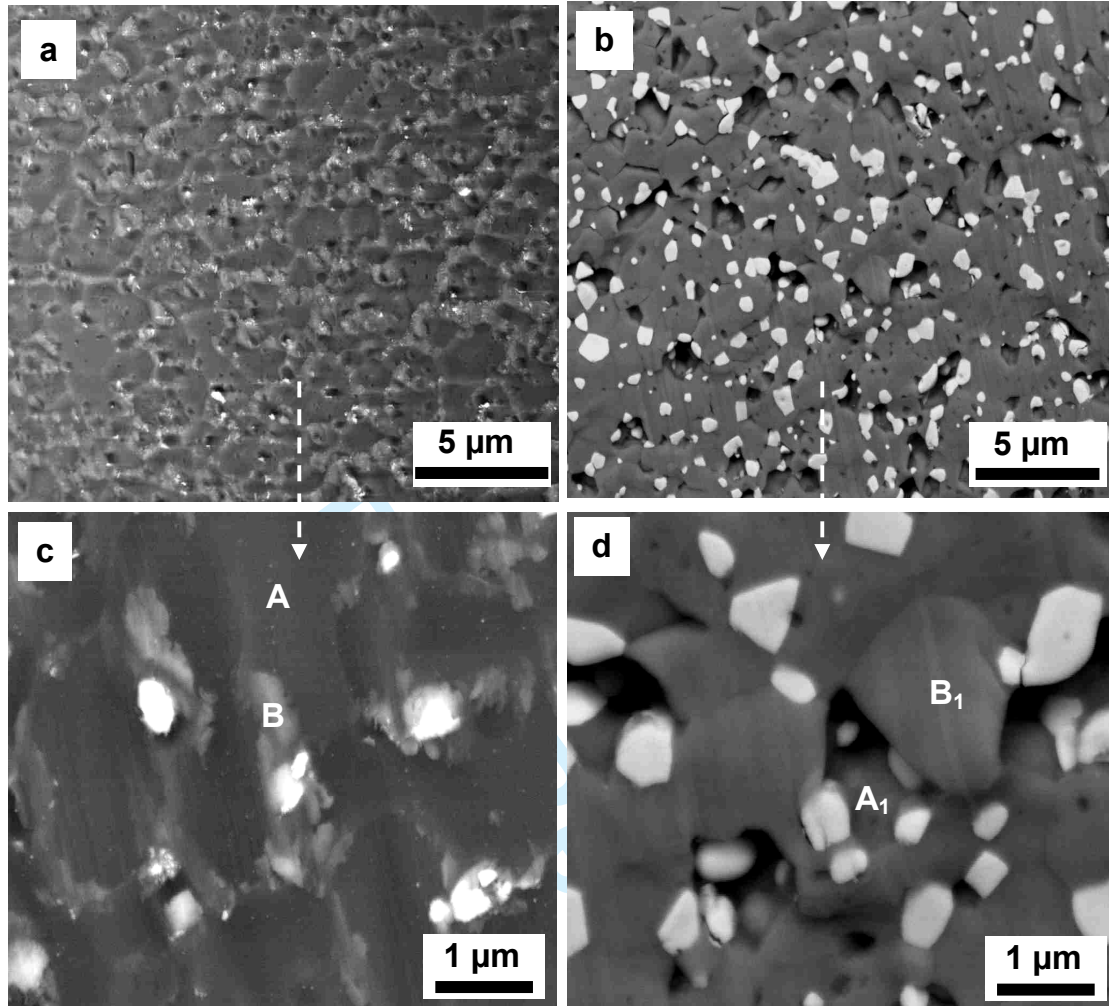


Fig. 6



**e**  
EDX-analysis (at.%):

	Ni	Al	O	Cr	Ta
<b>A</b>	2.1	34.0	63.9	0.0	0.0
<b>B</b>	7.4	29.6	61.5	1.4	0.1

**f**  
EDX-analysis (at.%):

	Ni	Al	O	Cr	Ta
<b>A<sub>1</sub></b>	56.3	31.6	9.2	2.7	0.2
<b>B<sub>1</sub></b>	37.6	26.5	34.5	1.1	0.2

Fig. 7

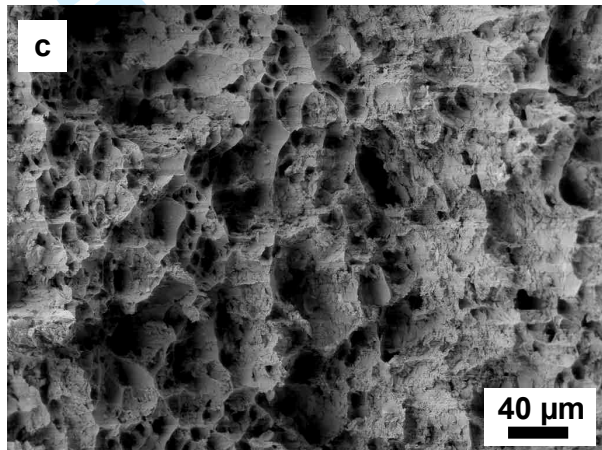
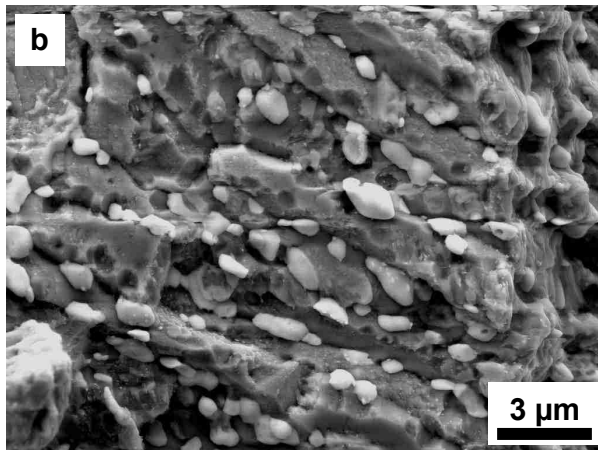
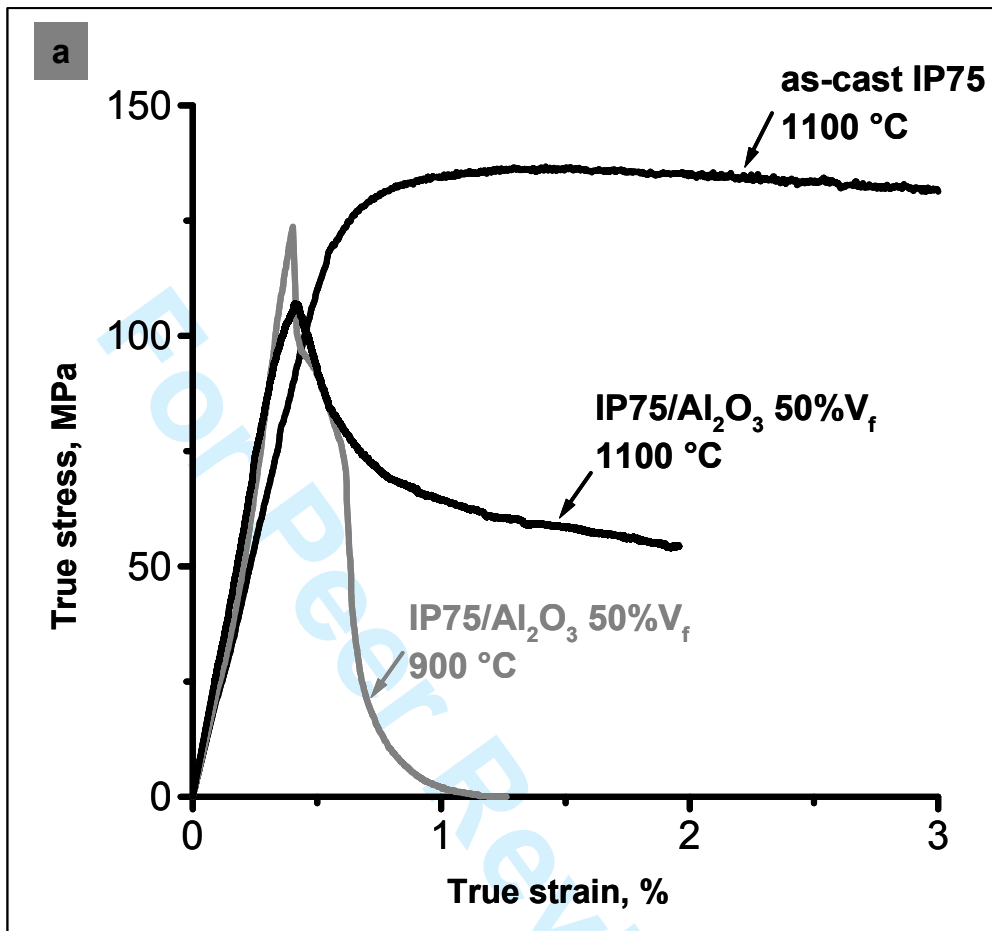


Fig. 8

